Direct Power Control Based on Dead-beat Function and Extended Kalman Filter for PV Systems

Mostafa Ahmed, *Member*, *IEEE*, Ibrahim Harbi, *Graduate Student Member*, *IEEE*, Ralph Kennel, *Senior Member*, *IEEE*, and Mohamed Abdelrahem, *Senior Member*, *IEEE*

***Abstract*—In this paper, a new proposal for the implementation of the well-known direct power control (DPC) technique in grid-connected photovoltaic (PV) systems is suggested. Normally, the DPC is executed using a look-up table procedure based on the error between the actual and reference values of the active and reactive power. Thus, the structure of the DPC is simple and results in a fast transient behavior of the inner current loop (injected currents). Therefore, in the current study, the DPC is reformulated using a dead-beat function. In this formulation, the reference voltage vector (RVV) is obtained in the α-β reference frame. Consequently, the switching states for the inverter can be obtained based on the sign of the components of the RVV. The suggested DPC is compared with the conventional one and other switching tables, which are intended for performance enhancement. Furthermore, an extended Kalman filter (EKF) is utilized to eliminate all grid-voltage sensors. Moreover, the switching frequency of the proposed technique is minimized without any need for weighting factors or cost function evaluation. The overall control technique is validated using a hardware-in-the-loop (HIL) experimental set-up and compared with other schemes under different operating conditions.**

***Index Terms*—Photovoltaic (PV) system, direct power control (DPC), sensorless control, switching frequency minimization, weighting factor.**

I. Introduction

RENEWABLE energy sources (RESs) are becoming dominant in the energy market [1], [2]. The fossil fuel sources are expected to diminish over the coming years. However, the main concern is the significant contribution of these sources to global warming, pollution, and emissions [1], [3]. Alternative sources from renewable energies include hydraulic, wind, and photovoltaic (PV). All these types of RESs are considered effective solutions to the problems that have arisen from conventional sources [1]. Among RESs, PV energy is attracting more attention [4], [5], which has several merits in comparison to other types of sources. For instant, the PV energy can be utilized for small- or large-scale power applications [6]. The PV energy is widely spread, i.e., special site properties are not a requirement as in the case of wind or hydraulic energies [7]. Furthermore, the PV sources can be integrated with the grid or for stand-alone applications, where the interconnection with the grid is difficult such as in remote and isolated areas. A commonly used application for such loads is the water pumping system for irrigation and drinking purposes [8], [9].

The RESs commonly use a two-stage structure, where the first stage is concerned with the maximum power point tracking (MPPT) technique. Popularly, this stage is dependent on the source of energy. For example, in a permanent-magnet synchronous generator based wind energy system, the first stage is a two-level converter. For PV sources, a boost converter is normally utilized to enable grid integration due to the voltage boosting capability. The second stage in different systems is usually a two-level inverter, and within this stage, the active and reactive power control is accomplished [1], [3].

To regulate the active and reactive power in grid-connected applications, the most commonly utilized schemes are the voltage-oriented control (VOC) and direct power control (DPC) [10]. In the VOC method, the active and reactive power exchanges with the grid are executed by aligning the grid-voltage vector along with the *d*-axis such that the active and reactive power are decoupled and can be separately controlled. Furthermore, the VOC contains two control loops, namely the voltage loop (outer) and the current loop (inner), where the outer loop provides the reference current to the inner loop [11], [12]. In another context, the outer voltage loop is corresponding to the active power component, where the *d*-axis reference current is proportional to the active power, and the *q*-axis current is based on the reactive power injection scheme [13]. By means of proportional-integral (PI) controllers, the reference voltage is computed and applied to the modulation stage, which implies the need for tuning efforts. In the DPC technique, a switching table is used to gen-

Manuscript received: December 7, 2021; revised: March 2, 2022; accepted: April 26, 2022. Date of CrossCheck: April 26, 2022. Date of online publication: June 27, 2022.

M. Ahmed (corresponding author), I. Harbi, R. Kennel, and M. Abdelrahem are with the Chair of High-Power Converter Systems (HLU), Technical University of Munich (TUM), 80333 Munich, Germany, M. Ahmed and M. Abdelrahem are also with the Department of Electrical Engineering, Faculty of Engineering, Assiut University, Assiut 71515, Egypt, and I. Harbi is also with the Department of Electrical Engineering, Faculty of Engineering, Menoufia University, Shebin El-Koum 32511, Egypt (e-mail: mostafa.ahmed@tum.de; ibrahim.harbi@tum.de; ralph.kennel@tum.de; mohamed.abdelrahem@tum.de).

DOI: 10.35833/MPCE.2021.000793

erate the actions of the power switches, where a hysteresis controller is utilized to compare the error signals between the actual and reference values of the active and reactive power [1], [3].

Recently, model predictive control techniques are getting more attention for different control objectives [14]. These techniques can be categorized into continuous-set model predictive control (CS-MPC), and finite-set model predictive control (FS-MPC) [15]. In the CS-MPC, a modulator is required to generate the switching states for the inverter. However, the FS-MPC relies on the discrete nature of the utilized topology, where a discrete-time model of the system under control is derived. And then the control parameter is predicted based on this model. After that, according to a cost function, the optimal switching state, which minimizes the difference between the predicted control parameter and its reference value, is selected. For example, for the two-level inverter, the cost function is evaluated 8 times (the possible switching vectors of the two-level inverter) to obtain the best switching state [14], [16]. Obviously, the FS-MPC requires high computation effort for implementation.

To this end, Table I summarizes different inverter control techniques, where the VOC, FS-MPC, and DPC are considered for comparison [17]-[19]. These control techniques vary from each other in different aspects including structure, implementation, tuning efforts, computational burden, etc. Nevertheless, DPC is considered the simplest technique with less tuning efforts and low calculation load. However, its steady-state response is unsatisfactory.

TABLE I
SUMMARY OF DIFFERENT INVERTER CONTROL TECHNIQUES

Technique	Construction	Switching frequency	Flexibility	Tuning effort	Coordination transformation	Multi-variable	PWM requirement	Computational burden	Transient behavior	Steady-state response
VOC	Cascaded PI controllers, and pulse width modulation (PWM)	Fixed	Constraints and multi-objective are hard to include	High (for PI controllers)	Yes	Coupled (active and reactive power decoupling is required)	Yes	Low	Slow	Excellent (small oscillations)
FS-MPC	Discrete-time model of the system, and cost function design	Variable	Constraints and multi-objective can be incorporated in the cost function	Moderate (for weighting factors)	No	Decoupled	No	High	Fast	Good (moderate oscillations)
DPC	Hysteresis controller, and look-up switching table	Variable	Constraints and multi-objective are hard to include	Simple (for hysteresis bands)	No	Decoupled	No	Low	Fast	Bad (large oscillations)

Various control techniques have been implemented in the literature to enhance the behavior of DPC. The main classification for such techniques is DPC with space vector modulation, DPC-based predictive control, and DPC with nonlinear controllers [19]. On one hand, DPC with predictive control can be applied using single-vector, two-vector, and three-vector techniques. In this regard, the high execution time related to the predictive techniques is considered the major drawback. Moreover, the aforementioned different vector implementation complicates the control technique. On the other hand, combining different non-linear controllers with the DPC such as sliding mode control [20] and fuzzy logic control [21] makes the DPC lose its simple structure. Additionally, the increased complexity adds to the demerits of these techniques.

Recently, sensorless control techniques are gaining more interest due to several advantages not only in terms of cost reduction for low-power applications but also the ability to ensure continuous operation of the system in case of sensor failure. Furthermore, noise elimination and simplification of the hardware requirement are significant and major features of sensorless control techniques [22]. Some efforts have been made to decrease the number of required sensors for the implementation of DPC. An estimation based on the instantaneous power theory is presented in [23], where the derivative of current is used to estimate the active and reactive power, which make it sensitive to the noise in measurements. In [24], a virtual-flux method is proposed, which is based on the analogy between the machine parameters and the grid-side filter. Therefore, the grid with a filter can be treated as a virtual AC motor. However, the sensitivity to DC drift and initial bias affect the performance of this technique [19], [25]. Additionally, some observers have been employed for grid-voltage sensor elimination such as sliding mode observer [26], and extended observer [27].

Considering the above, it is obvious that the DPC is simple without any tuning efforts. However, the conventional DPC suffers from high ripples in the steady-state, which deteriorate the quality of the injected currents. Therefore, we are motivated to sustain the simple principle of the DPC technique. In this regard, we propose a new formulation for the well-known DPC, where a dead-beat function is used to locate the optimal switching vector. In this function, the reference voltage is calculated in the α-β reference frame. Further on, the polarity of the two components of the reference voltage is used to set the switching actions without the need for hysteresis controllers or cost function evaluation. The

grid-voltage sensors (3 sensors) are eliminated by utilizing an extended Kalman filter (EKF). This, in turn, reduces the cost and enhances the system reliability. The EKF is an efficient estimator in addition to its ability for noise rejection and filtering capability. Therefore, it is chosen for implementation in this paper. Furthermore, the reduction of the switching frequency is accomplished using weighting factorless technique. The main contributions of the current study are summarized as follows.

1) The DPC technique is novelly proposed to enhance the steady-state behavior of the conventional techniques.

2) Sensor reduction is accomplished by employing an EKF, which is considered an effective and reliable backup strategy in case of sensor failure. Furthermore, the filtering behavior of the EKF is investigated.

3) The switching frequency of the two-level inverter is reduced using a weighting factorless technique, which simplifies the overall control strategy without the need for tuning efforts.

4) Hardware-in-the-loop (HIL) of the suggested control technique is realized. Furthermore, the investigation and comparison with the conventional DPC and its enhanced versions are also conducted.

The remainder of this paper is organized as follows. Section II presents the mathematical model of the single-stage PV system. The proposed DPC without grid-voltage sensors is investigated in Section III. The experimental assessment using HIL set-up is given in Section IV. Finally, the paper is concluded in Section V.

II. Methematical Model of Single-stage PV System

The single-stage PV system is considered as an example of the RESs. Simply, this system is represented by a DC source, a two-level inverter, an RL filter, and a power grid [28]. Undoubtedly, the PV source characteristics are nonlinear, which necessitates an MPPT method to exploit and trace the ultimate power from the source. However, the current study is concentrating on the inversion stage. Figure 1 shows the two-level inverter with a grid connection. The time-domain behavior of this circuit is characterized by:

$$v_{abc}=u_{abc}+L_f\frac{\mathrm{d}i_{abc}}{\mathrm{d}t}+R_f i_{abc} \tag{1}$$

where u_{abc} denotes the output voltage of the two-level inverter; v_{abc} denotes the grid voltage; i_{abc} denotes the flowing current; and L_f and R_f denote the filter parameters. This relation can be formulated in the α-β and d-q reference frames as [3]:

$$v_{\alpha\beta}=u_{\alpha\beta}+L_f\frac{\mathrm{d}i_{\alpha\beta}}{\mathrm{d}t}+R_f i_{\alpha\beta} \tag{2}$$

$$\begin{cases} v_d=u_d+L_f\dfrac{\mathrm{d}i_d}{\mathrm{d}t}+R_f i_d-\omega L_f i_q \\ v_q=u_q+L_f\dfrac{\mathrm{d}i_q}{\mathrm{d}t}+R_f i_q+\omega L_f i_d \end{cases} \tag{3}$$

where ω is the angular grid-frequency. Consequently, the expressions of active and reactive power at the same frames are:

$$\begin{cases} P=\dfrac{3}{2}(v_\alpha i_\alpha+v_\beta i_\beta) \\ Q=\dfrac{3}{2}(v_\beta i_\alpha-v_\alpha i_\beta) \end{cases} \tag{4}$$

$$\begin{cases} P=\dfrac{3}{2}(v_d i_d+v_q i_q) \\ Q=\dfrac{3}{2}(v_q i_d-v_d i_q) \end{cases} \tag{5}$$

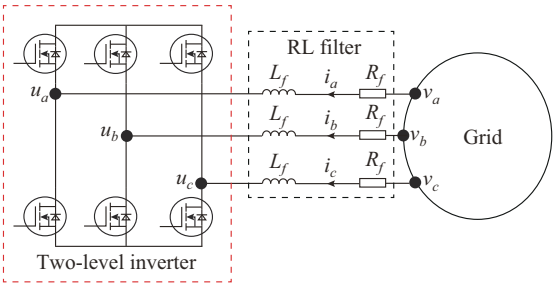

Fig. 1. Two-level inverter with grid integration.

III. Proposed DPC Without Grid-voltage Sensors

A. Concept of Proposed DPC

Conventionally, the DPC implementation depends on dividing the α-β reference frame into 12 sectors. Based on this sector distribution, the optimal switching state can be located using a predefined switching table. The inputs for this table are the hysteresis commands and the grid-voltage position. The digitized commands produced from the hysteresis controller are based on the error (hysteresis band) between the reference values of the power (active and reactive) and actual values [23].

In the proposed DPC, a dead-beat function is used to govern which switching vector is applied. The principles of the dead-beat function are investigated in [29]. However, it can be briefly described here with reference to (3), using the discrete form of this formula:

$$\begin{cases} i_d(k+1)=\left(1-\dfrac{T_s R_f}{L_f}\right)i_d(k)+\omega T_s i_q+\dfrac{T_s}{L_f}(v_d(k)-u_d(k)) \\ i_q(k+1)=\left(1-\dfrac{T_s R_f}{L_f}\right)i_q(k)-\omega T_s i_d+\dfrac{T_s}{L_f}(v_q(k)-u_q(k)) \end{cases} \tag{6}$$

where T_s is the sampling time; and $k+1$ and k are the future and present instants, respectively. According to dead-beat control [29], the current at the next instant is replaced with its reference value to force the controller to follow the reference. Therefore, the reference voltage vector (RVV) is obtained by rearranging (6):

$$u_{dref}(k)=-R_f i_d(k)-\frac{L_f}{T_s}(i_{dref}(k+1)-i_d(k))+\omega L_f i_q+v_d(k) \tag{7}$$

$$u_{qref}(k)=-R_f i_q(k)-\frac{L_f}{T_s}(i_{qref}(k+1)-i_q(k))-\omega L_f i_d+v_q(k) \tag{8}$$

where u_{dref} and u_{qref} are the components of the RVV in the d-q reference frame, respectively; and i_{dref} and i_{qref} are the compo-

nents of the reference current in the *d-q* reference frame, respectively.

To this end, Park transformation is used to calculate the RVV in the *α-β* reference frame as:

$$\boldsymbol{u}_{\alpha\beta ref}(k)=\begin{bmatrix}\cos\theta & \sin\theta\\ -\sin\theta & \cos\theta\end{bmatrix}\boldsymbol{u}_{dqref}(k) \tag{9}$$

where θ is the grid-voltage angle. It is worth mentioning that we prefer to derive the control law of the proposed strategy in the *d-q* reference frame to simplify the implementation for the two-stage PV system, where commonly the DC-link voltage controller gives the reference *d*-axis current to the inner loop. However, the execution in the *α-β* reference frame is simply feasible in the proposed strategy by discretizing (2) directly. This, in turn, removes the step of coordinates transformation.

The possible voltage vectors of the two-level inverter are given in Table II, where the output voltages in different frames are presented. Furthermore, the switching states corresponding to these vectors are included. With the help of Table II, and as the RVV is now already known, the output voltages of the two-level inverter in the *α-β* reference frame can be grouped into three categories as follows.

1) Zero voltage vectors, which are notated by $\boldsymbol{u}_0$ and $\boldsymbol{u}_7$.

2) Positive voltage vectors ($\boldsymbol{u}_1$, $\boldsymbol{u}_2$, and $\boldsymbol{u}_3$), where the summation of the two components of the output voltage is greater than 0 ($u_\alpha+u_\beta>0$).

3) Negative voltage vectors ($\boldsymbol{u}_4$, $\boldsymbol{u}_5$, and $\boldsymbol{u}_6$), for which $u_\alpha+u_\beta<0$.

TABLE II
SWITCHING STATES AND OUTPUT VOLTAGES OF TWO-LEVEL INVERTER IN *α-β* AND *abc* REFERENCE FRAMES

Voltage vector	Switching state $\boldsymbol{S}_{abc}$	Output voltages u_α, u_β	Output voltages u_a, u_b, u_c
$\boldsymbol{u}_0$	000	0, 0	0, 0, 0
$\boldsymbol{u}_1$	100	$\frac{2v_{dc}}{3}$, 0	$\frac{2v_{dc}}{3}$, $\frac{-v_{dc}}{3}$, $\frac{-v_{dc}}{3}$
$\boldsymbol{u}_2$	110	$\frac{v_{dc}}{3}$, $\frac{\sqrt{3}v_{dc}}{3}$	$\frac{v_{dc}}{3}$, $\frac{v_{dc}}{3}$, $\frac{-2v_{dc}}{3}$
$\boldsymbol{u}_3$	010	$\frac{-v_{dc}}{3}$, $\frac{\sqrt{3}v_{dc}}{3}$	$\frac{-v_{dc}}{3}$, $\frac{2v_{dc}}{3}$, $\frac{-v_{dc}}{3}$
$\boldsymbol{u}_4$	011	$\frac{-2v_{dc}}{3}$, 0	$\frac{-2v_{dc}}{3}$, $\frac{v_{dc}}{3}$, $\frac{v_{dc}}{3}$
$\boldsymbol{u}_5$	001	$\frac{-v_{dc}}{3}$, $\frac{-\sqrt{3}v_{dc}}{3}$	$\frac{-v_{dc}}{3}$, $\frac{-v_{dc}}{3}$, $\frac{2v_{dc}}{3}$
$\boldsymbol{u}_6$	101	$\frac{v_{dc}}{3}$, $\frac{-\sqrt{3}v_{dc}}{3}$	$\frac{v_{dc}}{3}$, $\frac{-2v_{dc}}{3}$, $\frac{v_{dc}}{3}$
$\boldsymbol{u}_7$	111	0, 0	0, 0, 0

As a result, the implementation of the DPC can be executed following this order:

1) If the calculated RVV equals zero, one of the zero voltage vectors is selected to be applied. In our design, $\boldsymbol{u}_0$ is selected. However, the other zero voltage vector $\boldsymbol{u}_7$ is used to minimize the switching frequency, which will be discussed in the following section.

2) If the computed RVV lies in the group of the positive voltage vectors, one vector from this group ($\boldsymbol{u}_1$, $\boldsymbol{u}_2$, and $\boldsymbol{u}_3$) will be adopted. Simply, if the two components of the RVV are positive, $\boldsymbol{u}_2$ is picked. However, if the u_α component is negative and the u_β component is positive, the switching state corresponding to $\boldsymbol{u}_3$ is chosen. Otherwise, $\boldsymbol{u}_1$ is nominated for application.

3) Similarly, $\boldsymbol{u}_5$ is applied for two negative components. $\boldsymbol{u}_6$ is enforced if u_β is negative and u_α is positive. Otherwise, $\boldsymbol{u}_4$ is placed in action.

B. Switching Frequency Minimization

As mentioned previously, in the present design, the voltage vector $\boldsymbol{u}_0$ is selected to be applied. However, if the previously switching state has two ones, i.e., the previous applied voltage vector is one of $\boldsymbol{u}_2$, $\boldsymbol{u}_4$, or $\boldsymbol{u}_6$, it is more convenient to consider the other zero voltage vector $\boldsymbol{u}_7$ for application. This reduces the number of commutations, and hence the switching frequency. Figure 2 shows the proposed algorithm for switching frequency minimization of the proposed DPC.

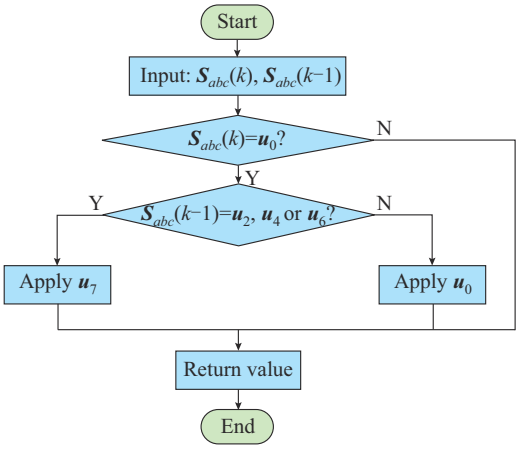

Fig. 2. Proposed algorithm for switching frequency minimization of proposed DPC.

C. Grid-voltage Estimation Based on EKF

In this subsection, the grid-voltage sensors are eliminated by utilizing an EKF, which is the nonlinear version of the Kalman filter [3]. Its design depends also on the discrete-time model of the system [3], [30]. Thus, the model of the system including disturbance can be written as:

$$\begin{cases}\dot{\boldsymbol{x}}=\boldsymbol{A}\boldsymbol{x}+\boldsymbol{B}\boldsymbol{u}+\boldsymbol{w}\\ \boldsymbol{y}=\boldsymbol{C}\boldsymbol{x}+\boldsymbol{D}\boldsymbol{u}+\boldsymbol{v}\end{cases} \tag{10}$$

where $\boldsymbol{x}=[i_\alpha, i_\beta, v_\alpha, v_\beta]^{\mathrm{T}}$ is the state vector; $\boldsymbol{u}=[\hat{v}_\alpha-u_\alpha, \hat{v}_\beta-u_\beta]^{\mathrm{T}}$ is the input, $\hat{v}_\alpha$ and $\hat{v}_\beta$ are the estimated grid voltages; $\boldsymbol{y}=[i_\alpha, i_\beta]^{\mathrm{T}}$ is the measurement; $\boldsymbol{w}$ denote the system uncertainties with covariance matrix $\boldsymbol{Q}$; and $\boldsymbol{v}$ is the measurement noise with covariance matrix $\boldsymbol{R}$. The covariance matrices $\boldsymbol{Q}$ and $\boldsymbol{R}$ are represented as:

$$\begin{cases}\boldsymbol{Q}=\mathrm{diag}(q_{11}, q_{22}, q_{33}, q_{44})\\ \boldsymbol{R}=\mathrm{diag}(r_{11}, r_{22})\end{cases} \tag{11}$$

Furthermore, $\boldsymbol{A}$, $\boldsymbol{B}$, $\boldsymbol{C}$, and $\boldsymbol{D}$ are the system matrices, which can be expressed as (with reference to (2)):

$$\begin{cases} \boldsymbol{A}=\begin{bmatrix} -\frac{R_f}{L_f} & 0 & 0 & 0 \\ 0 & -\frac{R_f}{L_f} & 0 & 0 \\ 0 & 0 & 0 & 0 \\ 0 & 0 & 0 & 0 \end{bmatrix} \\ \boldsymbol{B}=\begin{bmatrix} \frac{1}{L_f} & 0 \\ 0 & \frac{1}{L_f} \\ 0 & 0 \\ 0 & 0 \end{bmatrix} \\ \boldsymbol{C}=\begin{bmatrix} 1 & 0 & 0 & 0 \\ 0 & 1 & 0 & 0 \end{bmatrix} \\ \boldsymbol{D}=\boldsymbol{0} \end{cases} \tag{12}$$

Therefore, the discrete model can be expressed as:

$$\begin{cases} \boldsymbol{x}(k+1)=\boldsymbol{A}_d\boldsymbol{x}(k)+\boldsymbol{B}_d\boldsymbol{u}(k)+\boldsymbol{w}(k) \\ \boldsymbol{y}(k)=\boldsymbol{C}_d\boldsymbol{x}(k)+\boldsymbol{D}_d\boldsymbol{u}(k)+\boldsymbol{v}(k) \end{cases} \tag{13}$$

where $\boldsymbol{A}_d=\boldsymbol{I}+\boldsymbol{A}T_s$, and $\boldsymbol{I}$ is the identity matrix; $\boldsymbol{B}_d=\boldsymbol{B}T_s$; $\boldsymbol{C}_d=\boldsymbol{C}$; and $\boldsymbol{D}_d=\boldsymbol{D}$. Usually, the system uncertainty and measurement noise are not recognized, so the EKF is executed as:

$$\begin{cases} \hat{\boldsymbol{x}}(k+1)=\boldsymbol{A}_d\hat{\boldsymbol{x}}(k)+\boldsymbol{B}_d\boldsymbol{u}(k)+\boldsymbol{K}(k)(\boldsymbol{y}(k)-\hat{\boldsymbol{y}}(k)) \\ \hat{\boldsymbol{y}}(k)=\boldsymbol{C}_d\hat{\boldsymbol{x}}(k)+\boldsymbol{D}_d\boldsymbol{u}(k) \end{cases} \tag{14}$$

where $\boldsymbol{K}(k)$ is the Kalman gain; and $\hat{\boldsymbol{x}}(k)$ and $\hat{\boldsymbol{y}}(k)$ are the estimated values.

Finally, the implementation of the EKF can be carried out within two stages of prediction and modification. The prediction phase involves the state vector prediction $\hat{\boldsymbol{x}}^-(k)$ and the covariance matrix error prediction $\boldsymbol{P}^-(k)$ as follows.

$$\hat{\boldsymbol{x}}^-(k)=\boldsymbol{A}_d\hat{\boldsymbol{x}}(k-1)+\boldsymbol{B}_d\boldsymbol{u}(k-1) \tag{15}$$

$$\boldsymbol{P}^-(k)=\boldsymbol{f}(k)\boldsymbol{P}(k-1)\boldsymbol{f}(k)^{\mathrm{T}}+\boldsymbol{Q} \tag{16}$$

$$\boldsymbol{f}(k)=\left.\frac{\partial(\boldsymbol{A}_d\boldsymbol{x}(k)+\boldsymbol{B}_d\boldsymbol{u}(k))}{\partial\boldsymbol{x}}\right|_{\hat{\boldsymbol{x}}^-(k)} \tag{17}$$

where $\boldsymbol{f}(k)$ contains the partial derivatives of the state vector elements with respect to each other. In another context, it is defined as the Jacobian matrix and is expressed as:

$$\boldsymbol{f}(k)=\begin{bmatrix} 1-\frac{T_sR_f}{L_f} & 0 & \frac{T_s}{L_f} & 0 \\ 0 & 1-\frac{T_sR_f}{L_f} & 0 & \frac{T_s}{L_f} \\ 0 & 0 & 1 & 0 \\ 0 & 0 & 0 & 1 \end{bmatrix} \tag{18}$$

The modification or correction stage is formulated as:

$$\boldsymbol{K}(k)=\boldsymbol{P}^-(k)\boldsymbol{C}_d^{\mathrm{T}}(\boldsymbol{C}_d\boldsymbol{P}^-(k)\boldsymbol{C}_d^{\mathrm{T}}+\boldsymbol{R})^{-1} \tag{19}$$

$$\hat{\boldsymbol{x}}(k)=\hat{\boldsymbol{x}}^-(k)+\boldsymbol{K}(k)(\boldsymbol{y}(k)-\boldsymbol{C}_d\hat{\boldsymbol{x}}^-(k)) \tag{20}$$

$$\boldsymbol{P}(k)=\boldsymbol{P}^-(k)-\boldsymbol{K}(k)\boldsymbol{C}_d\boldsymbol{P}^-(k) \tag{21}$$

To this end, the grid voltages are replaced with their estimated values in (7) and (8). By doing so, a reduced sensor count is achieved (3 sensors are eliminated), which greatly reduces the cost and enhances the system reliability. The whole system setup and proposed DPC technique for single-stage PV system are illustrated in Fig. 3.

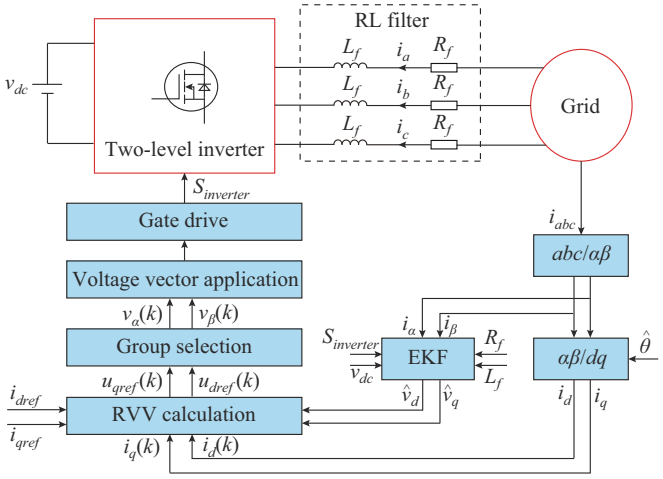

Fig. 3. System set-up and proposed DPC technique for single-stage PV system.

IV. Experimental Assessment Using HIL Setup

A. System Specifications and Description

The system under consideration consists of a DC source and a two-level inverter interfaced to the power grid via an RL filter. The system is built using HIL arrangement (RT Box CE). The real-time controller is implemented utilizing dSPACE MicroLabBox, where the voltage and current measurements are fed to the analog inputs of the controller. Furthermore, the switching actions are enforced to the digital inputs of the box. The HIL setup simplifies testing the system under different operating conditions. The configuration of the implemented system is shown in Appendix A Fig. A1. Table III gives the parameters of the grid-connected single-stage PV system.

TABLE III
Parameters of Grid-connected Single-stage PV System

Parameter	Value
DC input voltage (v_{dc})	700 V
Filter resistance (R_f)	0.25 Ω
Filter inductance (L_f)	20 mH
Grid-voltage (v)	400 V
Grid-frequency (f)	50 Hz
Sampling time (T_s)	100 µs

B. Evaluation and Discussions

Several attempts have been proposed to enhance the behavior of the conventional DPC by modifying the switching table. In this regard, the proposed method is compared with the conventional DPC, the first modified switching table [31] (Table *m*1), and the second adjusted switching table [32] (Table *m*2) under different operating conditions.

The system response is investigated at step changes of the active power (P), and the reference of the reactive power (Q) is set to be zero to achieve unity power factor operation. The performance of the system is studied for three levels of active power variation, which are zero power level, 5 kW power level, and 10 kW power level.

Figure 4 shows the transient behavior of different DPC techniques, namely the conventional DPC, the modified tables, and the proposed one, where the active power, reactive power, and *abc* currents are illustrated, respectively. The active power oscillations of the conventional DPC and Table $m1$ are very similar. However, Table $m2$ has higher power ripples in comparison with the conventional DPC and Table $m1$. This is further investigated in the steady-state response of the DPC techniques, as is shown in Fig. 5. The ripple content of the active power with the proposed DPC is the smallest among all studied techniques. Furthermore, the peak value of the active power is higher for the proposed technique evaluated against other DPC techniques. Further on, the reactive power oscillations of the conventional DPC and Table $m1$ are comparable together. The reactive power ripple content of Table $m2$ exhibits a significant improvement in comparison with the conventional technique and Table $m1$, especially at higher active power values, where the offset of the reactive power from its reference value (zero) is very noticeable for the conventional method and Table $m1$. The proposed DPC has the finest behavior when considering reactive power oscillation, where the reactive power is approximately centered around its reference value. Table IV gives the average values of the injected active and reactive power. The average active power (at 10 kW level) for the proposed DPC is the highest among all DPC techniques. However, Table $m2$ average power is the lowest. The gained average value with the proposed method is approximately 0.5 kW in comparison with the conventional DPC, which represents an increase of around 4.4%.

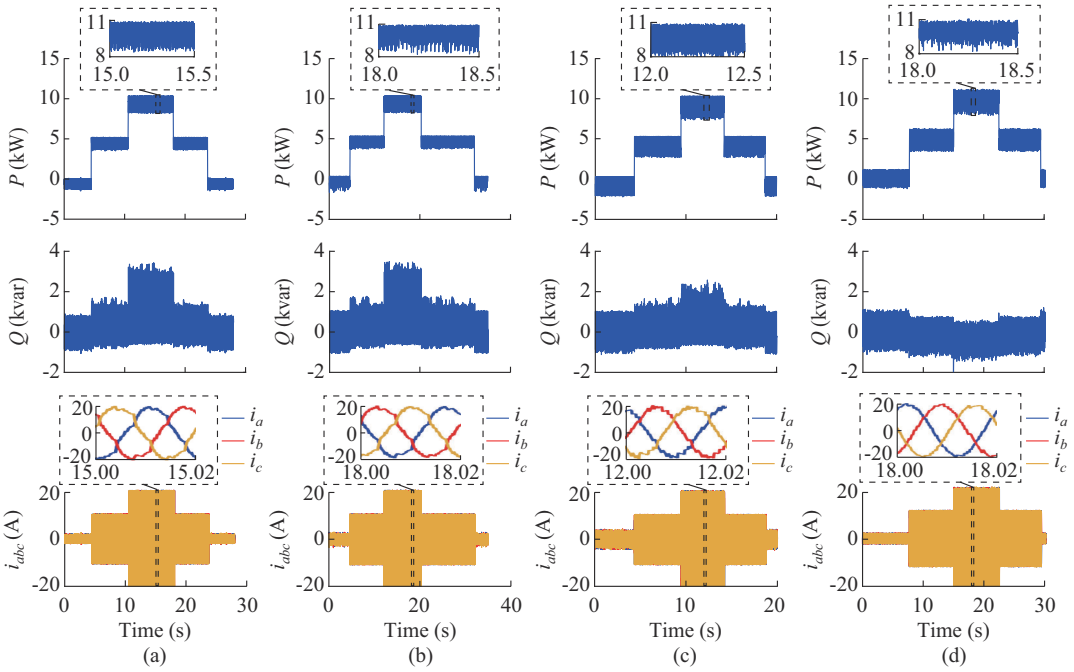

Fig. 4. Transient behavior of different DPC techniques. (a) Conventional DPC. (b) Table $m1$. (c) Table $m2$. (d) Proposed DPC.

TABLE IV
COMPARISON AMONG DPC TECHNIQUES WITH REGARD TO P AND Q

Technique	Average active power (kW)	Average reactive power (var)
Conventional DPC	9.52	317.67
Table $m1$	9.52	378.17
Table $m2$	9.23	188.80
Proposed DPC	9.94	–232.46

Regarding the steady-state behavior of the conventional DPC in Fig. 5, especially the original one, it is obvious that the active and reactive power track their references in a poor manner. In fact, this is the cause of average power reduction and distorted currents. This phenomenon is also reported in the literature [21], [29], where large spikes of active and reactive power occur. The poor control behavior of the original DPC is due to the poor tracking of the active power during odd sectors and reactive power during even sectors [29]. Figure 5 also shows that the reactive power with the proposed DPC has a small offset with respect to the reference value. This is mainly due to the operation without grid-voltage sensors. However, even with sensor elimination, the behavior of the proposed DPC is better than the conventional ones, where large spikes can be observed in the reactive power waveform. In brief, according to the switching tables of the conventional DPC, the selection of the switching states is still inappropriate [21]. However, the proposed DPC is able to pick the optimal switching vector using the adopted dead-beat function, where its principle is clear and intuitive.

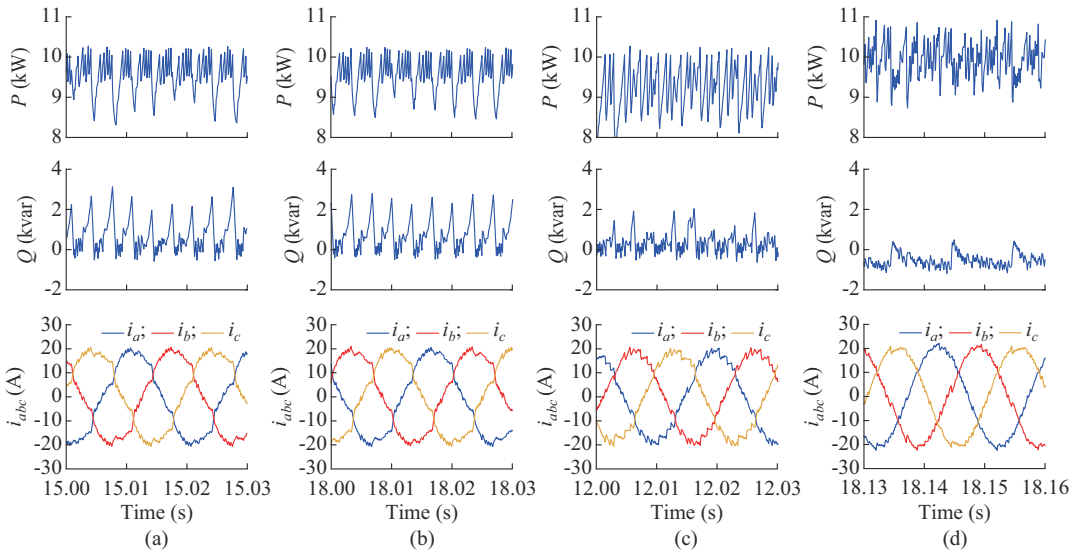

Fig. 5. Steady-state behavior of different DPC techniques. (a) Conventional DPC. (b) Table *m*1. (c) Table *m*2. (d) Proposed DPC.

Moreover, the injected *abc* currents with the proposed DPC are more sinusoidal. Table V presents the total harmonic distortion (THD) values of *abc* currents for all DPC techniques at 10 kW power level, where the proposed DPC has the minimum THD among all techniques. The THD value of other DPC techniques is approximately doubled compared with the proposed one.

TABLE V
THD VALUES OF *abc* CURRENTS FOR ALL TECHNIQUES AT 10 KW POWER LEVEL

Technique	THD (%)
Conventional DPC	9.62
Table *m*1	9.37
Table *m*2	8.28
Proposed DPC	4.87

It is worth mentioning that the proposed DPC gives superior performance in all aspects compared with the other DPC techniques despite grid-voltage sensors elimination. Further insight is given to assess the performance of the DPC techniques, where the execution time and average switching frequency f_s of all techniques are investigated in Table VI. The proposed DPC gives a little bit lower average switching frequency. However, the computation load of the proposed DPC is higher than others due to grid-voltage estimation using EKF. The calculation time of the proposed DPC without grid-voltage elimination is 9.59 μs, which is comparable to other DPC techniques.

To verify the outstanding performance of the proposed DPC, the conventional and modified DPC techniques are evaluated at a lower sampling time. To be specific, the sampling time is reduced to the half (50 μs) and the response of the DPC techniques is revisited at the same previous step response.

In Fig. 6, it can be observed that the behavior of the conventional and modified DPC techniques is enhanced (as expected because of sampling reduction). At the first glance, the conventional DPC and Table *m*1 give a similar behavior. Furthermore, Table *m*2 response is further enhanced and is better than the conventional DPC and Table *m*1. Table VII provides a comparison among these techniques at the above-mentioned sampling time. The average switching frequency of the conventional and modified DPC techniques is almost doubled with THD improvement. However, the THD enhancement is not significant for the conventional DPC and Table *m*1. But for Table *m*2, the improvement is clear. The behavior of the proposed DPC is remarkable, where the THD of the currents is improved with switching frequency minimization in comparison with other techniques. To this end, and with reference to Tables V, VI, and VII, the proposed DPC presents the most superior performance among all studied techniques, where it gives a better THD for the currents, higher injected average power, and lower switching frequency.

TABLE VI
EXECUTION TIME AND AVERAGE SWITCHING FREQUENCY OF DPC TECHNIQUES

Technique	Execution time (s)	f_s (kHz)
Conventional DPC	8.98	1.49
Table *m*1	8.97	1.49
Table *m*2	9.16	1.48
Proposed DPC	18.19	1.44

C. Further Investigation on Performance of Proposed DPC Using EKF Estimation

In this subsection, the behavior of the proposed DPC without grid-voltage sensors is inspected. Figure 7 shows the measured and the estimated grid-voltages in the α-β reference frame using EKF estimation. The estimation of the grid-voltages is very satisfactory. However, a delay can be observed in the waveform due to the digital controller. This delay is compensated in the implemented algorithm. Furthermore, the actual and the estimated currents are revealed in

Fig. 8. The estimation is adequate. However, the ripple content of the estimated currents is smaller compared with the actual ones. This is clarified in Fig. 9, where the variation of the currents around the peak is smoother for the estimated case. As a result, the THD value of the estimated current is improved compared with the measured one. Table VIII gives a summary of the THD values of the actual and estimated currents using the proposed DPC, where a reduction of 0.5% is achieved for the estimated currents. This is due to the filtering behavior of the EKF, which is a relevant feature, especially for noisy measurements. It is worth mentioning that the values of the covariance matrices used in the experimental implementation are given as:

$$\begin{cases} \boldsymbol{Q} = \text{diag}(0.01, 0.01, 25, 25) \\ \boldsymbol{R} = \text{diag}(1, 1) \end{cases} \tag{22}$$

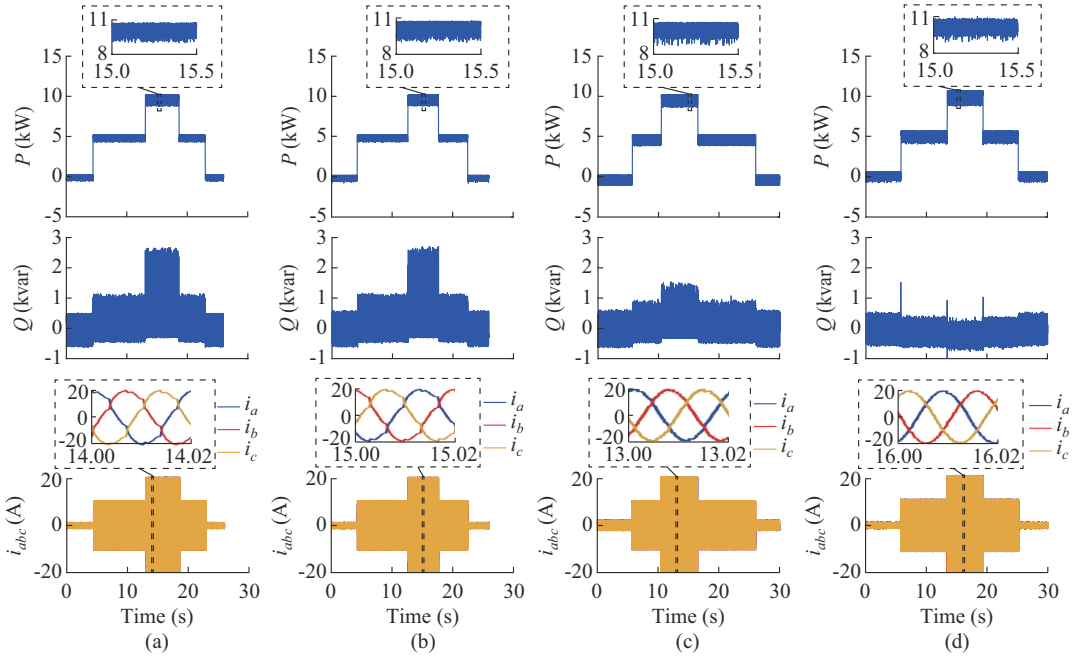

Fig. 6. Transient behavior of DPC techniques under step change of active power at 50 μs sampling time. (a) Conventional DPC. (b) Table *m*1. (c) Table *m*2. (d) Proposed DPC.

TABLE VII
COMPARATIVE EVALUATION FOR CONVENTIONAL AND MODIFIED DPC TECHNIQUES AT 50 μS

Technique	THD (%)	f_s (kHz)
Conventional DPC	7.16	2.93
Table *m*1	7.05	2.83
Table *m*2	4.13	2.76
Proposed DPC	2.95	2.65

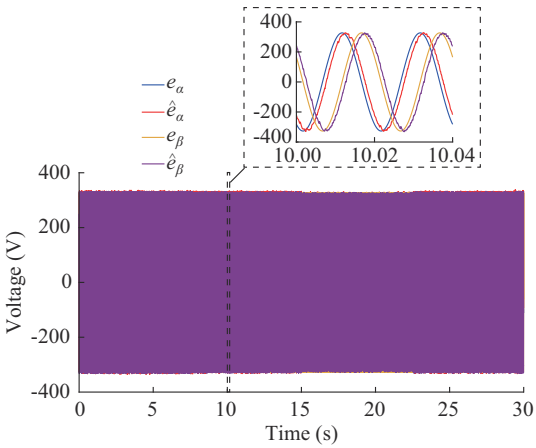

Fig. 7. Measured and estimated grid-voltages using EKF.

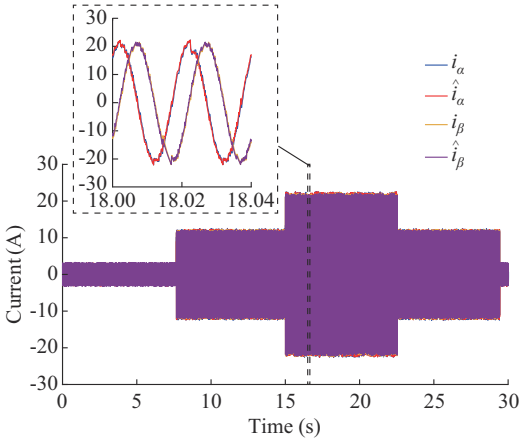

Fig. 8. Actual and estimated currents using EKF.

To verify the effectiveness of the EKF estimation, a case study is investigated, where a step-down change in the grid-voltage and grid-frequency is applied to the system. To be specific, the voltage and frequency are both decreased to 80% of their nominal values. The estimation of the voltage, in this case, is shown in Fig. 10, where the EKF can follow the variation of the grid-voltage and grid-frequency in a very short time and without any effect on the system's behavior.

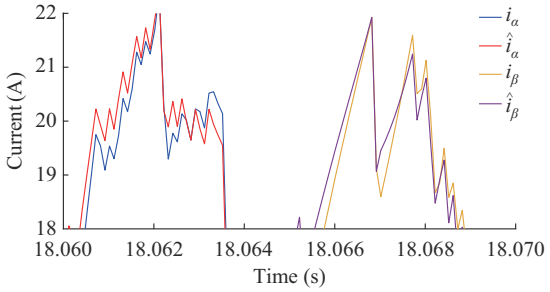

Fig. 9. Steady-state response of actual and estimated currents using EKF.

TABLE VIII
THD VALUES OF ACTUAL AND ESTIMATED CURRENTS USING PROPOSED DPC

Case	THD (%)
Actual current	4.87
Estimated current	4.27

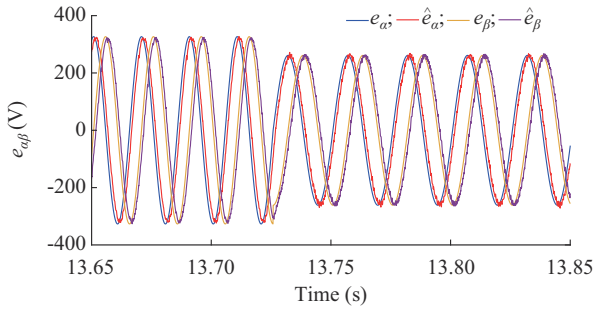

Fig. 10. Measured and estimated grid-voltages under step change of grid-voltage and grid-frequencies.

The average switching frequency of the proposed DPC with and without switching minimization is further investigated in Table IX. The proposed procedure for switching frequency reduction succeeds to accomplish around 16.28% reduction in the average value. It is worth mentioning that this reduction is calculated within a short span. Therefore, and over a long time operation, the reduction is expected to be higher. This, in turn, reduces the switching losses without any significant effect on the quality of the injected currents.

TABLE IX
AVERAGE SWITCHING FREQUENCY OF PROPOSED DPC WITH AND WITHOUT SWITCHING MINIMIZATION

Technique	f_s (kHz)
Proposed DPC without switching minimization	1.72
Proposed DPC with switching minimization	1.44

V. CONCLUSION

A new implementation for the DPC is suggested in this paper based on a dead-beat function, where the computed RVV is used as a guide to select the best switching state. The polarity of the components of the RVV in the α-β reference frame gives a simple directory to adopt the optimal switching vector. Unlike the conventional DPC, the proposed DPC can be executed without the need for a predefined switching table or hysteresis controller. Furthermore, switching frequency minimization is accomplished, in which no weighting factor is required. The grid-voltage sensors are eliminated by employing an EKF, where an accurate estimation of the voltages and currents is achieved. The comparative evaluation among the conventional DPC techniques and the proposed one udner different conditions indicates an elegant performance of the suggested methodology even when conventional techniques operate at lower sampling time. The proposed DPC achieves about 16.28% switching frequency reduction. Furthermore, the EKF is considered an effective backup strategy in case of sensor failure in addition to its filtering capability.

APPENDIX A

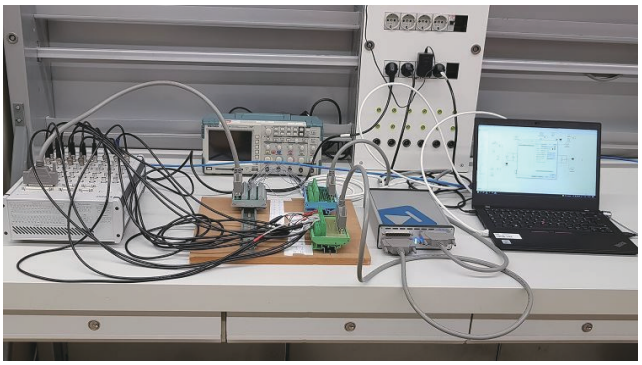

Fig. A1. Configuration of implemented system.

REFERENCES

[1] M. Ahmed, M. Abdelrahem, A. Farhan *et al.*, "DC-link sensorless control strategy for grid-connected PV systems," *Electrical Engineering*, vol. 103, pp. 2345-2355, Feb. 2021.
[2] S. Sajadian and R. Ahmadi, "Distributed maximum power point tracking using model predictive control for photovoltaic energy harvesting architectures based on cascaded power optimizers," *IEEE Journal of Photovoltaics*, vol. 7, no. 3, pp. 849-857, May 2017.
[3] M. Ahmed, M. Abdelrahem, and R. Kennel, "Highly efficient and robust grid connected photovoltaic system based model predictive control with Kalman filtering capability," *Sustainability*, vol. 12, no. 11, p. 4542, Jun. 2020.
[4] M. H. Ahmadi, M. Ghazvini, M. Sadeghzadeh *et al.*, "Solar power technology for electricity generation: a critical review," *Energy Science & Engineering*, vol. 6, no. 5, pp. 340-361, Sept. 2018.
[5] S. Lyden, H. Galligan, and M. E. Haque, "A hybrid simulated annealing and perturb and observe maximum power point tracking method," *IEEE Systems Journal*, vol. 15, no. 3, pp. 4325-4333, Sept. 2020.
[6] J. Khan and M. H. Arsalan, "Solar power technologies for sustainable electricity generation – a review," *Renewable & and Sustainable Energy Reviews*, vol. 55, pp. 414-425, Mar. 2016.
[7] F. Blaabjerg, Y. Yang, D. Yang *et al.*, "Distributed power-generation systems and protection," *Proceedings of the IEEE*, vol. 105, no. 7, pp. 1311-1331, Jun. 2017.
[8] M. A. Elgendy, B. Zahawi, and D. J. Atkinson, "Assessment of perturb and observe MPPT algorithm implementation techniques for PV pumping applications," *IEEE Transactions on Sustainable Energy*, vol. 3, no. 1, pp. 21-33, Jan. 2012.
[9] M. A. Elgendy, B. Zahawi, and D. J. Atkinson, "Comparison of directly connected and constant voltage controlled photovoltaic pumping systems," *IEEE Transactions on Sustainable Energy*, vol. 1, no. 3, pp. 184-192, Oct. 2010.
[10] K. Zeb, W. Uddin, M. A. Khan *et al.*, "A comprehensive review on inverter topologies and control strategies for grid connected photovoltaic system," *Renewable & Sustainable Energy Reviews*, vol. 94, pp. 1120-1141, Oct. 2018.

[11] R. Kadri, J. Gaubert, and G. Champenois, "An improved maximum power point tracking for photovoltaic grid-connected inverter based on voltage-oriented control," *IEEE Transactions on Industrial Electronics*, vol. 58, no. 1, pp. 66-75, Jan. 2011.
[12] V. Kumar and M. Singh, "Derated mode of power generation in PV system using modified perturb and observe MPPT algorithm," *Journal of Modern Power Systems and Clean Energy*, vol. 9, no. 5, pp. 1183-1192, Sept. 2021.
[13] Y. Yang and H. Wen, "Adaptive perturb and observe maximum power point tracking with current predictive and decoupled power control for grid-connected photovoltaic inverters," *Journal of Modern Power Systems and Clean Energy*, vol. 7, no. 2, pp. 422-432, Mar. 2019.
[14] S. Vazquez, J. Rodriguez, M. Rivera *et al*., "Model predictive control for power converters and drives: advances and trends," *IEEE Transactions on Industrial Electronics*, vol. 64, no. 2, pp. 935-947, Feb. 2017.
[15] A. Lashab, D. Sera, J. M. Guerrero *et al*., "Discrete model-predictive-control-based maximum power point tracking for PV systems: overview and evaluation," *IEEE Transactions on Power Electronics*, vol. 33, no. 8, pp. 7273-7287, Aug. 2018.
[16] J. Rodriguez, M. P. Kazmierkowski, J. R. Espinoza *et al*., "State of the art of finite control set model predictive control in power electronics," *IEEE Transactions on Industrial Informatics*, vol. 9, no. 2, pp. 1003-1016, May 2013.
[17] S. Kouro, P. Cortes, R. Vargas *et al*., "Model predictive control – a simple and powerful method to control power converters," *IEEE Transactions on Industrial Electronics*, vol. 56, no. 6, pp. 1826-1838, Jun. 2009.
[18] F. Wang, Z. Zhang, X. Mei *et al*., "Advanced control strategies of induction machine: field oriented control, direct torque control and model predictive control," *Energies*, vol. 11, no. 1, p. 120, Jan. 2018.
[19] S. Yan, Y. Yang, S. Hui *et al*., "A review on direct power control of pulsewidth modulation converters," *IEEE Transactions on Power Electronics*, vol. 36, no. 10, pp. 11984-12007, Oct. 2021.
[20] J. Hu, L. Shang, Y. He *et al*., "Direct active and reactive power regulation of grid-connected DC/AC converters using sliding mode control approach," *IEEE Transactions on Power Electronics*, vol. 26, no. 1, pp. 210-222, Jan. 2011.
[21] A. Bouafia, F. Krim, and J. Gaubert, "Fuzzy-logic-based switching state selection for direct power control of three-phase PWM rectifier," *IEEE Transactions on Industrial Electronics*, vol. 56, no. 6, pp. 1984-1992, Jun. 2009.
[22] A. Rahoui, A. Bechouche, H. Seddiki *et al*., "Grid voltages estimation for three-phase PWM rectifiers control without AC voltage sensors," *IEEE Transactions on Power Electronics*, vol. 33, no. 1, pp. 859-875, Jan. 2018.
[23] T. Noguchi, H. Tomiki, S. Kondo *et al*., "Direct power control of PWM converter without power-source voltage sensors," *IEEE Transactions on Industry Applications*, vol. 34, no. 3, pp. 473-479, Jun. 1998.
[24] M. Malinowski, M. P. Kazmierkowski, S. Hansen *et al*., "Virtual-flux-based direct power control of three-phase PWM rectifiers," *IEEE Transactions on Industry Applications*, vol. 37, no. 4, pp. 1019-1027, Aug. 2001.
[25] X. Chen, W. Wu, N. Gao *et al*., "Finite control set model predictive control for LCL-filtered grid-tied inverter with minimum sensors," *IEEE Transactions on Industrial Electronics*, vol. 67, no. 12, pp. 9980-9990, Dec. 2020.
[26] X. Xiao, Y. Zhang, X. Song *et al*., "Virtual flux direct power control for PWM rectifiers based on an adaptive sliding mode observer," *IEEE Transactions on Industry Applications*, vol. 54, no. 5, pp. 5196-5205, Oct. 2018.
[27] Z. Song, Y. Tian, Z. Yan *et al*., "Direct power control for three-phase two-level voltage-source rectifiers based on extended-state observation," *IEEE Transactions on Industrial Electronics*, vol. 63, no. 7, pp. 4593-4603, Jul. 2016.
[28] J. Hu, J. Zhu, and D. G. Dorrell, "Model predictive control of grid-connected inverters for PV systems with flexible power regulation and switching frequency reduction," *IEEE Transactions on Industry Applications*, vol. 51, no. 1, pp. 587-594, Feb. 2015.
[29] A. Bouafia, J. Gaubert, and F. Krim, "Predictive direct power control of three-phase pulse width modulation (PWM) rectifier using space-vector modulation (SVM)," *IEEE Transactions on Power Electronics*, vol. 25, no. 1, pp. 228-236, Jan. 2010.
[30] M. Abdelrahem, C. M. Hackl, Z. Zhang *et al*., "Robust predictive control for direct-driven surface-mounted permanent-magnet synchronous generators without mechanical sensors," *IEEE Transactions on Energy Conversion*, vol. 33, no. 1, pp. 179-189, Mar. 2018.
[31] A. Bouafia, J. Gaubert, and F. Krim, "Analysis and design of new switching table for direct power control of three-phase PWM rectifier," in *Proceedings of 13th International Power Electronics and Motion Control Conference*, Poznan, Poland, Sept. 2008, pp. 703-709.
[32] A. Baktash, A. Vahedi, and M. A. S. Masoum, "Improved switching table for direct power control of three-phase PWM rectifier," in *Proceedings of Australasian Universities Power Engineering Conference*, Perth, Australia, Jun. 2008, pp. 1-5.

Mostafa Ahmed received the B.Sc. (Hons.) and M.Sc. degrees in electrical engineering from Assiut University, Assiut, Egypt, in 2010 and 2015, respectively. He is currently working toward the Ph. D. degree at the Chair of High-Power Converter Systems (HLU), Technical University of Munich (TUM), Munich, Germany. His research interests include renewable energy systems, modeling of photovoltaic systems, maximum power point tracking (MPPT), predictive control of power electronics converters, and sensorless control of photovoltaic systems.

Ibrahim Harbi received the B.Sc. (Hons.) and M.Sc. degrees in electrical engineering from Menoufia University, Shebin El-Koum, Egypt, in 2012 and 2016, respectively. He is currently working toward the Ph.D. degree at the Chair of High-Power Converter Systems (HLU), Technical University of Munich (TUM), Munich, Germany. His research interests include multilevel converter topologies and control, predictive control of power electronics converters, and photovoltaic energy systems.

Ralph Kennel received the Diploma and Dr.-Ing. (Ph.D.) degrees in electrical engineering from the University of Kaiserslautern, Kaiserslautern, Germany, in 1979 and 1984, respectively. From 1983 to 1999, he worked on several positions with Robert BOSCH GmbH, Gerlingen, Germany. From 1994 to 1999, he was a Visiting Professor at the University of Newcastle-upon-Tyne, Newcastle-upon-Tyne, U.K.. From 1999-2008, he was Professor for Electrical Machines and Drives at Wuppertal University, Wuppertal, Germany. Since 2008, he is a Professor for electrical drive systems and power electronics at Technical University of Munich, Munich, Germany. He is a Fellow of the Institution of Electrical Engineers (IEE) and a Chartered Engineer in the U.K.. Within the IEEE, he is the Treasurer of the Germany Section as well as the ECCE Global Partnership Chair of the Power Electronics Society. His main research interests include sensorless control of AC drives, predictive control of power electronics, and hardware-in-the-loop systems.

Mohamed Abdelrahem received the B.Sc. (Hons.) and M.Sc. degrees in electrical engineering from Assiut University, Assiut, Egypt, in 2007 and 2011, respectively, and the Ph.D. degree (Hons.) in electrical engineering from the Technical University of Munich (TUM), Munich, Germany, in 2020. Since 2019, he is the Head of research group "Renewable Energy Systems" at the Chair of High-Power Converter Systems (HLU), TUM. Since 2020, he is an Assistant Professor at the Electrical Engineering Department, Assiut University. He is recorded in world's top 2% scientist's list by Stanford University. His research interests include power electronics, predictive and encoderless control of variable-speed wind generators, photovoltaic energy systems, and energy storage systems.